

# APPLICATION OF THEORETICAL MODELS TO ACTIVE AND PASSIVE REMOTE SENSING OF SALINE ICE

# N93-13086

H. C. Han, J. A. Kong, R. T. Shin

Massachusetts Institute of Technology, Cambridge, Massachusetts

S. V. Nghiem, and R. Kwok

Jet Propulsion Laboratory, California Institute of Technology, Pasadena, California

**Abstract**—The random medium model is used to interpret the polarimetric active and passive measurements of saline ice. The ice layer is described as a host ice medium embedded with randomly distributed inhomogeneities, and the underlying sea water is considered as a homogeneous half-space. The scatterers in the ice layer are modeled with an ellipsoidal correlation function. The orientation of the scatterers is vertically aligned and azimuthally random. The strong permittivity fluctuation theory is employed to calculate the effective permittivity and the distorted Born approximation is used to obtain the polarimetric scattering coefficients. We also calculate the thermal emissions based on the reciprocity and energy conservation principles. The effects of the random roughness at the air-ice, and ice-water interfaces are accounted for by adding the surface scattering to the volume scattering return incoherently. The above theoretical model, which has been successfully applied to analyze the radar backscatter data of the first-year sea ice near Point Barrow, AK, is used to interpret the measurements performed in the CRRELEX program.

interfaces, and add incoherently to the volume scattering return obtained with the distorted Born approximation. This model has been successfully applied to study the radar backscatter for the thick first-year sea ice data measured near Point Barrow, Alaska [5]. In this study, we further employ this model to interpret the multi-frequency active and passive measurements taken during the CRRELEX experiment.

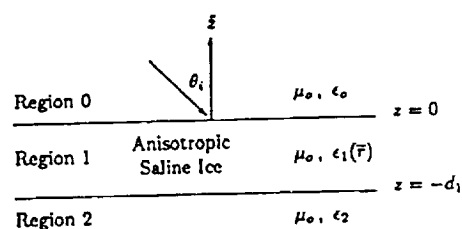


Figure 1 Scattering configuration.

## INTRODUCTION

Understanding electromagnetic wave interaction with saline ice provides physical insight for interpretation of active and passive remote sensing data of sea ice. Various theoretical models have been developed to characterize the scattering and the emission properties of sea ice [1]. In this paper, the random medium model [2] is used to interpret the measurement data collected at the US Army Cold Regions Research and Engineering Laboratory (CRREL) under the CRRELEX program. To simulate sea ice, saline ice was grown under partially controlled condition at CRREL and active and passive microwave signatures of the saline ice were measured together with ice characteristic parameters.

Under quiescent condition, the background ice grows in columnar form and saline water is trapped between ice platelets in the form of brine inclusions which are usually ellipsoidal. The ice tends to grow vertically downward rendering the ellipsoidal inclusions aligned preferably in the vertical direction and the crystallographic *c*-axes parallel to the horizontal plane. In this case, the *c*-axes are, however, random in the horizontal direction. The saline ice layer is modeled as a random medium containing ellipsoidal scatterers vertically aligned but randomly oriented in the horizontal direction. The strong fluctuation theory is employed to calculate the effective permittivity and the distorted Born approximation is used to obtain the polarimetric scattering coefficients. The emissivity of a layer of sea ice overlying sea water can be obtained through the principles of reciprocity and energy conservation [3]. In other words, the emissivity is obtained as one minus the reflectivity. To account for the effects of rough interfaces, we use small perturbation method [4] to evaluate the surface scattering from air-ice, and ice-water

## MODEL DESCRIPTION

### Multi-Layered Random Medium Model

The fully polarimetric multi-layered random medium model for sea ice has been developed with the wave theory. The layer configuration is shown in Fig. 1. Region 0 represents the homogeneous air above sea ice. The sea ice in region 1 contains vertically aligned ellipsoidal scatterers such as saline ice with brine pockets or air bubbles which has spatially varying permittivity  $\epsilon_1(\vec{r})$ . Region 2 is the underlying sea water with homogeneous permittivity  $\epsilon_2$ . All three regions are assumed to have the free-space permeability  $\mu_0$ .

An exponential correlation function locally corresponding to a scatterer is used in the derivation of the effective permittivity with the strong fluctuation theory extended to account for the ellipsoidal shape and the horizontally random orientation of the scatterers. The local correlation function of the brine inclusion has three different correlation lengths related to the three different axial lengths of the ellipsoid as shown in Fig. 2. The azimuthal orientation of the scatterer is depicted locally with the local  $z'$ -axis parallel to the global  $z$ -axis and an Eulerian fluctuation angle  $\phi_f$  corresponding to the angle between the *c*-axis and the global horizontal axis (*x*-axis). When the average process is performed over the random orientation angle  $\phi_f$ , the effective permittivity is a uniaxial tensor with vertical optic axis describing the effective azimuthal symmetry of the inhomogeneous sea ice. When a single set of correlation lengths is used, for simplicity, to model the brine inclusions with various sizes, these correlation lengths are considered as related to the effective size of the scatterers. After the effective permittivity of the sea ice is calculated, the complete set of polarimetric scattering coefficients are obtained under the distorted Born



approximation with the anisotropic dyadic Green's function for the layer media. From the scattering coefficients, the Mueller matrix is computed to plot the polarization signatures of sea ice.

Under the distorted Born approximation the polarimetric scattering coefficients, obtained as the correlation of the scattered field, takes the form

$$\begin{aligned} \langle \bar{E}_{0s}(\bar{r}) \cdot \bar{E}_{0s}^*(\bar{r}) \rangle = & \sum_{i,j,k,l,m} k_o^4 \int_0^{2\pi} d\phi_f p(\phi_f) \int_{V_1} d\bar{r}_1 \int_{V_1} d\bar{r}_1^o C_{\xi n j k l m}(\bar{r}_1, \bar{r}_1^o; \phi_f) \\ & \left[ \langle G_{01ij}(\bar{r}, \bar{r}_1) \rangle \langle F_{1k}(\bar{r}_1) \rangle \right] \cdot \left[ \langle G_{01il}(\bar{r}, \bar{r}_1^o) \rangle \langle F_{1m}(\bar{r}_1^o) \rangle \right]^* \end{aligned} \quad (1)$$

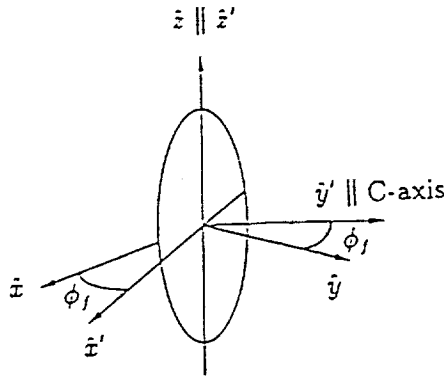


Figure 2 Geometry of scatterer in region 1.

where the uniaxial effective permittivity  $\bar{\epsilon}_{eff1}$  for region 1 is used to calculate the mean dyadic Green's functions and the mean fields  $\langle \bar{F}_1(\bar{r}) \rangle$ . The correlation function for region 1,  $C_{\xi 1 j k l m}(\bar{r}_1, \bar{r}_1^o; \phi_f)$  in (1) is the  $jklm$ -th element of fourth-rank correlation tensor  $\bar{\bar{C}}_{\xi 1}(\bar{r}_1, \bar{r}_1^o; \phi_f)$  defined as

$$C_{\xi 1 j k l m}(\bar{r}_1, \bar{r}_1^o; \phi_f) = \langle \xi_{1jk}(\bar{r}_1) \xi_{1lm}^*(\bar{r}_1^o) | \phi_f(\bar{r}_1) \rangle \quad (2)$$

In (1), the probability density function of scatterer orientation  $p(\phi_f)$  is simply

$$p(\phi_f) = \frac{1}{2\pi} \quad (3)$$

for complete random orientation horizontally with no preference in azimuthal direction, and  $k_o = \omega \sqrt{\mu_o \epsilon_o}$  is the free-space wavenumber with angular frequency  $\omega$ .

### Effective Permittivities

The strong fluctuation theory is used to derive the effective permittivities of the ice layer. The singularities of the dyadic Green's functions in the bilocal approximated Dyson's equations are accounted for; and the low-frequency approximation is applied to obtain the results for the anisotropic sea ice media. The derivations are done in the frequency domain with the Fourier-transform method.

The ice layer is described with a normalized local correlation function of the form

$$R_{\xi 1}(\bar{r}) = \exp \left( - \sqrt{ \frac{x^2}{\ell_x^2} + \frac{y^2}{\ell_y^2} + \frac{z^2}{\ell_z^2} } \right) \quad (4)$$

with correlation length  $\ell_x$ ,  $\ell_y$ , and  $\ell_z$  in the local coordinates corresponding to the minor, the meridian, and the major axes of

the scatterer. In this model, the correlation lengths are related to the effective size and shape of the scatterers. The effective permittivity of the ice layer is composed of a quasi-static part and a scattering part which accounts for the modification in the wave speed and attenuation

$$\bar{\epsilon}_{eff1} = \bar{\epsilon}_{g1} + \epsilon_o \left[ \bar{T} - \bar{\epsilon}_{eff1} \cdot \langle \bar{S}_1 \rangle \right]^{-1} \cdot \bar{\epsilon}_{eff1} \quad (5)$$

The effective dyadic scatterer  $\bar{\epsilon}_{eff1}$  is obtained from the volume integration of the dyadic Green's function and the correlation function, the auxiliary permittivity  $\bar{\epsilon}_{g1}$  and dyadic coefficient  $\bar{S}_1$  characterizing the source singularity of the dyadic Green's function are determined by the condition of secular term elimination.

### Scattering Coefficients

For polarimetric backscattering, the scattering coefficients are defined by

$$\sigma_{\mu\nu\tau\kappa} = \lim_{\substack{r \rightarrow \infty \\ A \rightarrow \infty}} \frac{4\pi r^2 \langle E_{\mu s} E_{\nu s}^* \rangle}{A E_{\tau i} E_{\kappa i}^*} \quad (6)$$

where  $A$  is the illuminated area, subscript  $i$  is for the incident wave,  $s$  represents the scattered wave, and  $\mu$ ,  $\nu$ ,  $\tau$ , and  $\kappa$  can be  $h$  or  $v$  which respectively stands for the horizontal or vertical components of the electric fields. The components of the scattered field in (6) are obtained by measuring the  $h$  and the  $v$  returns while the incident field is transmitted exclusively with  $h$  or  $v$  polarization. For backscattering from reciprocal media, the  $h$  return obtained by transmitting  $v$  is the same as the  $v$  return obtained by transmitting  $h$ .

### Rough Surface Contribution

To account for the effects of rough interfaces at  $z = 0$  and  $z = -d_1$ , we first approximate the surface statistics by a Gaussian correlation function with standard deviation  $\sigma$  and correlation length  $\ell$ , then employ the small perturbation method to obtain the first-order backscattering field from the interfaces. For example, the surface scattering from the air-ice interface is given by

$$\sigma_{hh} = 4k_o^4 \sigma^2 \ell^2 \cos^4 \theta_i \left| R_{01}^{TE} \right|^2 e^{-k_o^2 \ell^2 \sin^2 \theta_i} \quad (7a)$$

$$\begin{aligned} \sigma_{vv} = & 4k_o^8 \sigma^2 \ell^2 \cos^4 \theta_i \\ & \times \left| \frac{(k_1^2 - k_o^2)(k_1^2 \sin^2 \theta_i + k_{1z}^2)}{(k_1^2 k_z + k_o^2 k_{1z})^2} \right|^2 e^{-k_o^2 \ell^2 \sin^2 \theta_i} \end{aligned} \quad (7b)$$

where  $\theta_i$  and  $k_1$  denote the angle of incidence and the wavenumber for the ice layer, respectively. The surface scattering is incoherently added to the volume scattering return calculated based on the method described previously.

### Emissivities

The Kirchhoff law is invoked to obtain the emissivity of sea ice under isothermal condition from the active bistatic scattering coefficients.

$$e_h(\theta, \phi) = 1 - \frac{1}{4\pi} \sum_{b=h,v} \int_{4\pi} d\Omega' \gamma_{bh}(\theta', \phi'; \theta, \phi) \quad (8a)$$

$$e_v(\theta, \phi) = 1 - \frac{1}{4\pi} \sum_{b=h,v} \int_{4\pi} d\Omega' \gamma_{bv}(\theta', \phi'; \theta, \phi) \quad (8b)$$



where  $\gamma_{bh}(\theta', \phi'; \theta, \phi)$  represents the bistatic scattering coefficient for an  $h$ -polarized incident wave propagating in the direction described by  $(\theta, \phi)$  and scattered into the  $(\theta', \phi')$  direction with  $b$ -polarization.

## DATA INTERPRETATION

The theoretical results from the random medium model are compared to the CRRELEX data. For the case under consideration, region 0 is air, region 1 is the sea ice layer containing ellipsoidal brine inclusions, and region 2 is sea water. The thickness of the ice layer is obtained by ground truth measurement. The fractional volume of the brine inclusions is calculated from the bulk ice salinity and temperature. Results from publications are used to estimate the frequency-dependent permittivities of the ice background, the brine inclusions, and the underlying sea water. The theoretical calculations performed with and without the rough interfaces contributions are compared.

The local correlation lengths, which are not defined in the same manner as the global correlation lengths in the Perovich's estimation, corresponding to the effective size of the scatterers need to be determined. In our preliminary calculations, instead of adjusting the correlation lengths to match the experimental data, they are chosen from the characterization of the first-year sea ice obtained by a comparison with the 9 GHz measurements made at Point Barrow, Alaska [2]. This approach, based on the theoretical model, also serves the purpose of referring the remote sensing signatures of the saline ice artificially grown at CRREL to the sea ice in the natural conditions.

The theoretically calculated emissivities are in good agreement with the data. This indicates that the estimated effective permittivity tensor, which affects the emissivity even in the zeroth order, are close to that for natural sea ice. At lower frequencies where the electromagnetic wave can penetrate the ice, the emissivities can be sensitive to the ice thickness. In this case, the  $h$  polarization is more sensitive to the thickness than the  $v$  polarization which usually has higher attenuation. For information pertaining more to the first or higher order effects, active signatures should be considered.

The backscattering coefficients generated theoretically have also been compared with that observed in the CRRELEX experiment for co-polarized and cross-polarized returns only, since measurements of other elements in the covariance matrix are not available. At 5 GHz, the theoretical results overestimate the CRRELEX data at larger incident angles. This indicates that the local correlation lengths of the grown sea ice probably smaller than those observed at Point Barrow. At smaller incident angles, the measurements are higher than the theoretical values without rough surface contributions. At 10 GHz, the results, calculated using the above correlation lengths, are all higher than the measured values provided to us for the backscattering from the CRRELEX experiment.

## ACKNOWLEDGMENT

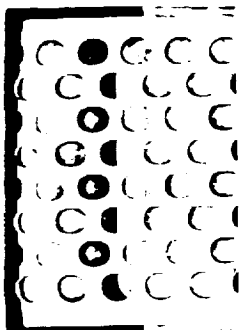
This work was supported by the ONR Contract No. N00014-89-J-1107, the NASA Grant No. NAGW-1617, and the NASA Contract No. 958461.

## REFERENCES

- [1] L. Tsang, J. A. Kong, and R. T. Shin, *Theory of Microwave Remote Sensing*, Wiley-Interscience, New York, 1985.
- [2] S. V. Nghiem, "Electromagnetic wave models for polarimetric remote sensing of geophysical media," *Ph.D. Thesis*, Massachusetts Institute of Technology, Cambridge, Massachusetts, 1991.
- [3] W. H. Peake, "Interaction of electromagnetic waves with some natural surfaces," *IEEE Trans. Ant. Propagat.*, Vol. AP-7, 5324-5329, 1959.
- [4] J. A. Kong, *Electromagnetic Wave Theory*, Second edition, Wiley-Interscience, New York, 1990.
- [5] Y. S. Kim, R. K. Moore, and R. G. Onstott, "Theoretical and experimental study of radar backscatter from sea ice," *RSL Tech. Report*, 331-337, University of Kansas Center for Research, Inc., Lawrence, Kansas, 1984.

ORIGINAL PAGE IS  
OF POOR QUALITY





## Scattering of Electromagnetic Waves from a Dense Medium Consisting of Correlated Mie Scatterers with Size Distributions and Applications to Dry Snow

L. Tsang

Electromagnetics and Remote Sensing Laboratory  
Department of Electrical Engineering  
University of Washington  
Seattle, WA 98195, USA

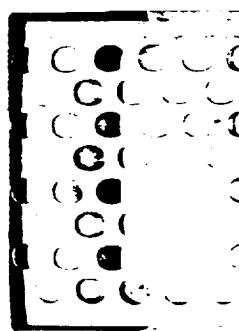
J. A. Kong

Department of Electrical Engineering and Computer Science  
Massachusetts Institute of Technology  
Cambridge, MA 02139, USA

**Abstract**— The scattering of a plane electromagnetic wave obliquely incident on a layer of dense medium consisting of dielectric spherical particles of finite sizes and with size distributions is studied. The spherical particles are of sizes comparable to wavelength so that Mie scattering is used to describe the single particle scattering characteristics. The coherent wave is studied with quasicrystalline approximation using the cross pair distribution functions of multiple sizes governed by Percus-Yevick approximation. The incoherent scattered wave is calculated with the distorted Born approximation with the result expressed in terms of a product of the T-matrices of particles of different sizes and permittivities and the Fourier transform of the cross pair distribution functions. The coherent wave effective propagation constants, the attenuation rates and the backscattering coefficients are illustrated numerically, with examples chosen to illustrate microwave and millimeter wave scattering from snow cover in the frequency range of 5 GHz to 95 GHz, and mean grain radius between 0.03 cm to 0.09 cm. Salient features of the numerical results for scattering from snow with size distribution are: 1. Correlated dense medium scattering is less than independent scattering at low frequency, a fact that is consistent with controlled laboratory experiment. 2. Scattering from dense medium of a Rayleigh size distribution with an average radius can be much larger than the case of monodisperse particles of the sizes identical to that average radius. 3. The scattering attenuation rate increases rapidly with frequency at low frequency regime and begins to level off at high frequency regime. 4. The coherent wave scattering attenuation rate is large in snow at frequencies above 15 GHz indicating large optical thickness and the importance of multiple scattering. Comparisons with extinction measurements of dry snow at 18 GHz, 35 GHz, 60 GHz, and 90 GHz are made.

### I. INTRODUCTION

Propagation and scattering in dense media has applications in remote sensing of geophysical terrain and nondestructive evaluation of composite materials [1-13]. In a dense medium, particles occupy an appreciable fractional volume. A main feature of a medium with densely packed scatterers is that Foldy's approximation [14]

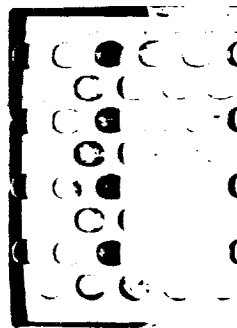
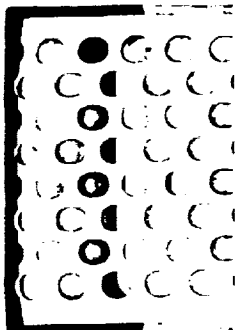


which has been successful in propagation problems through sparse media, is not applicable. It has been shown theoretically [1-2,4-6,9,15-16] and through laboratory experiments [3] that the effects of correlated scattering between scatterers must be taken into account.

Propagation and scattering in dense media has been studied with the quasicrystalline approximation [1-2,4-6], and the quasicrystalline approximation with coherent potential [6-8] for the first moment of the field and the correlated ladder approximation for the second moment of the field [7,9,13]. The dense medium theory is developed for media with particles of finite sizes. Because of the finite sizes of the particles, their positions are correlated. The dense medium radiative transfer theory has also been developed from these approximations to study multiple scattering effects in the incoherent wave. Some of the studies of correlated scattering have been limited to the case of low frequency [7,9] and/or particles of identical sizes [1-2,4-6,10-11]. However, to approximate physical reality in geophysical terrain scattering, size distributions of particles must be taken into account. The case of monodisperse particles and polydisperse scattering generally can give different results for independent scattering [14,17] as well as correlated scattering [8,16]. High frequency results are also important for example at frequencies above 15 GHz for snow cover.

In this paper, we study the scattering of a plane electromagnetic wave obliquely incident on a layer of dense medium consisting of dielectric spherical particles with size distributions. The spherical particles are of sizes comparable to wavelength so that Mie scattering is used to describe the single particle scattering characteristics. Thus the theory is applicable to particles of arbitrary size. The coherent wave is studied with the quasicrystalline approximation using the cross pair distribution functions of multiple sizes governed by Percus-Yevick approximation [18-20]. The integral equation of the quasicrystalline approximation gives rise to the generalized Lorentz-Lorentz law and the generalized Ewald-Oseen extinction theorem [4,21]. The generalized Lorentz-Lorentz law consists of a homogeneous system of equations. The resulting dispersion relation is an equation governing the effective propagation constant for the coherent wave. The generalized Ewald-Oseen extinction theorem is an inhomogeneous equation that relates the transmitted coherent field to the amplitude, polarization, and direction of propagation of the incident field. The name "generalized" denotes the fact that the classical Lorentz-Lorentz law and the Ewald-Oseen extinction theorem were derived for low frequency effective permittivity for the total field with the imaginary part accounting for absorption loss only. In the present "generalized" case, the effective propagation constant is derived for high frequency when the particle sizes are comparable to wavelength. Also the imaginary part of the effective propagation constant includes attenuation due to scattering diverted to other directions as well as absorption.

The calculations of the cross pair distribution functions are based on a special case of Percus-Yevick approximation that has no inter-particle forces except for non-interpenetration [8,17-19,22]. The Percus-Yevick cross pair distribution functions of multiple sizes have recently been shown to compare very well with Monte-Carlo simulations [23]. The incoherent scattered wave is calculated with





the distorted Born approximation with the result expressed in terms of a product of the T-matrices of particles of different sizes and permittivities and the Fourier transform of the cross pair distribution functions. Numerical examples are chosen to illustrate microwave and millimeter wave scattering from snow cover in the frequency range of 5 GHz to 95 GHz and mean grain radius ranging from 0.03 cm to 0.09 cm [24]. The Rayleigh size distribution and the modified gamma size distribution are used to illustrate the scattering. Salient features of the numerical results for scattering from snow with Rayleigh size distribution are: 1. Correlated dense medium scattering is less than independent scattering at low frequency that is consistent with controlled laboratory experiment [3]. 2. Scattering from dense medium of a Rayleigh size distribution with an average radius can be much larger than the case of monodisperse particles of the sizes identical to that average radius. Particles with larger size can contribute to scattering even though they are fewer in number. 3. The scattering attenuation rate increases rapidly with frequency at low frequency regime and begins to level off at high frequency regime. This is to be contrasted with Rayleigh scattering where scattering attenuation just increases rapidly with frequency. 4. The coherent wave scattering attenuation rate can be large at frequencies above 15 GHz based on the Rayleigh size distribution indicating large optical thickness and the importance of multiple scattering in snow at high frequencies. Comparisons are made with extinction measurements of dry snow at 18 GHz, 35 GHz, 60 GHz, and 90 GHz. Good agreement is obtained and the dense media theory is shown to be able to account for the frequency dependence of extinction of dry snow from 18 GHz to 90 GHz.

## II. FORMULATION

Consider a plane electromagnetic plane wave impinging in direction  $(\pi - \theta_i, \phi_i)$  upon a half space of spherical discrete scatterers of multiple sizes and multiple permittivities (Fig. 1). Let  $s_j$  be the species index  $j = 1, 2, \dots, L$ . Each species is described by the permittivity  $\epsilon_{s_j}$ , radius  $a_{s_j}$  and number density  $n_{s_j}$ . The number density  $n_{s_j}$  is related to the volume fraction of species  $f_{s_j}$ ,  $f_{s_j} = 4\pi n_{s_j} a_{s_j}^3 / 3$ . The scatterers are embedded in the lower half space (region 1) with background permittivity equal to  $\epsilon$  which is the same permittivity as that of the region 0 (Fig. 1).

The electric field of the incident wave is given by

$$\bar{E}_i(\bar{r}) = (E_{vi}\hat{\theta}_{id} + E_{hi}\hat{\phi}_i) e^{i\bar{k}_{id}\cdot\bar{r}} \quad (1)$$

where subscripts  $v$  and  $h$  denote vertical and horizontal polarizations respectively,  $\bar{k}_{id}$  denotes the downward propagating incident wave vector and  $\hat{\theta}_{id}$  and  $\hat{\phi}_i$  are the associated polarization vectors

$$\bar{k}_{id} = k(\sin \theta_i \cos \phi_i \hat{x} + \sin \theta_i \sin \phi_i \hat{y} - \cos \theta_i \hat{z}) \quad (2)$$

$$= k_{ix} \hat{x} + k_{iy} \hat{y} - k_{iz} \hat{z}$$

$$\hat{\theta}_{id} = -\hat{x} \cos \theta_i \cos \phi_i - \hat{y} \cos \theta_i \sin \phi_i - \hat{z} \sin \theta_i \quad (3)$$

$$\hat{\phi}_i = -\hat{x} \sin \phi_i + \hat{y} \cos \phi_i \quad (4)$$

In the following, our notation follows that of [6], pp. 446-454 and pp. 506-517. Under the quasicrystalline approximation for multiple species, the coherent field obeys the equation

$$\bar{w}^{(s_l)}(\bar{r}_l) = \sum_{s_j=1}^L n_{s_j} \int_{V_{jl}} d\bar{r}_j g_{s_j s_l}(\bar{r}_j - \bar{r}_l) \bar{\sigma}(k\bar{r}_l \bar{r}_j) \bar{T}^{(s_j)} \bar{w}^{(s_j)}(\bar{r}_j) + e^{i\bar{k}_{id} \cdot \bar{r}_l} \bar{a}_{inc} \quad (5)$$

where  $\bar{w}^{(s_l)}(\bar{r}_l)$  is the conditional average of the exciting field of particles at  $\bar{r}_l$  of species  $s_l$  conditioning on the particle at  $\bar{r}_l$ ,  $\bar{T}^{(s_j)}$  is the matrix representation of the  $T$  matrix of species  $s_j$  and  $\bar{\sigma}(k\bar{r}_l \bar{r}_j)$  is a transformation matrix transforming from vector spherical waves with center at  $\bar{r}_j$  to vector spherical waves with center at  $\bar{r}_l$  as given on p. 452 of [6]. It is an exact wave transformation applicable to near field, intermediate field, and far field regions. The function  $g_{s_j s_l}(\bar{r}_j - \bar{r}_l)$  is the cross pair distribution function of two species  $s_j$  and  $s_l$ . These can be computed readily from the Percus-Yevick approximation. These were originally derived for molecular dynamics of fluid mixtures. The result that we use is the special case when intermolecular forces are zero, and molecules cannot interpenetrate each other. In (5) the volume of integration  $V_{jl}$  for  $d\bar{r}_j$  is the lower half space excluding a "hole" of radius  $(a_{s_j} + a_{s_l})$  around vector  $\bar{r}_l$ . This is because

$$g_{s_j s_l}(\bar{r}_j - \bar{r}_l) = 0, \quad \text{for } |\bar{r}_j - \bar{r}_l| < a_{s_j} + a_{s_l} \quad (6)$$

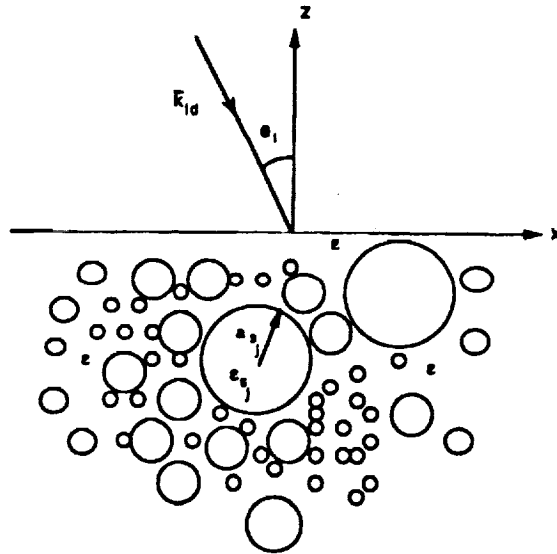


Figure 1. Geometry of the problem: an incident electromagnetic plane wave impinging upon a dense medium consisting of spherical particles with a size distribution.

In (5)  $\bar{a}_{inc}$  is the column matrix representing the coefficients of the incident wave when expanded into spherical waves, as given on pp. 507 and 514 of [6].

To solve (5), we assume the solution

$$\bar{w}^{(s_1)}(\bar{r}_l) = \bar{a}_E^{(s_1)} e^{i\bar{K}_d \bar{r}_l} \quad (7)$$

where  $\bar{a}_E^{(s_1)}$  is a column matrix representing coefficients of the exciting field and  $\bar{K}_d$  is the downward going effective wave vector

$$\bar{K}_d = K_x \hat{x} + K_y \hat{y} - K_z \hat{z} \quad (8)$$

and the effective wavenumber is

$$K = \sqrt{K_x^2 + K_y^2 + K_z^2} \quad (9)$$

Substitution of (7) into the integrand of the integral (5), integrations can be performed [4,6]. The integral yields two terms that correspond to two waves with dependencies

$$e^{i\bar{K}_d \bar{r}_l} \quad (10)$$

and

$$e^{iK_x x_l + iK_y y_l - i(k^2 - K_x^2 - K_y^2)^{1/2} z_l} \quad (11)$$

The first wave given by (10) propagates with  $\bar{K}_d$  and is to be balanced with the term  $\bar{w}^{(s_1)}(\bar{r}_l)$  on the left hand side of equation since they both have the same propagation constant. Balancing these two terms give rise to the generalized Lorentz-Lorentz law which can be used to calculate the effective propagation constant  $K$ . The second wave of (11) with incident wave wavenumber  $k$  in the square root will cancel the second term on the right hand side of (5) which is the incident wave term. This cancellation or extinction is the generalized Ewald-Oseen extinction theorem [6,25]. For the two terms to cancel out, the wave vector of (11) must exactly balance the incident wave vector. This gives rise to the phase matching condition

$$K_x = k_{ix} \quad (12)$$

$$K_y = k_{iy} \quad (13)$$

so that from (8), (9), (10), we obtain Snell's law for the effective propagation constant,

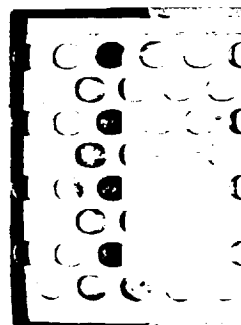
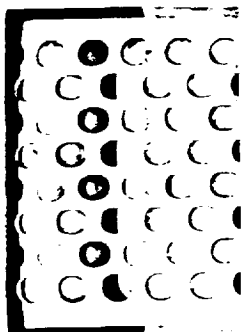
$$K \sin \theta_t = k \sin \theta_i \quad (14)$$

$$K_z = (K^2 - k^2 \sin^2 \theta_i)^{1/2} \quad (15)$$

We call both laws generalized because the concept has been generalized to coherent wave at high frequency while the classical laws were derived for low frequency case.

#### A. Generalized Lorentz-Lorentz Law

The  $\bar{a}_E^{(s_1)}$  column matrix for the exciting field can be expressed in terms of  $Y_n^{(s_j)(M)}$  and  $Y_n^{(s_j)(N)}$  coefficients where  $(M)$  stands for  $\bar{M}$  type of vector spherical wave and  $(N)$  stands for  $\bar{N}$  type of vector spherical wave and  $n$  is the



multipole index. The  $Y_n^{(s_j)(M)}$  and  $Y_n^{(s_j)(N)}$  coefficients satisfy a homogeneous set of equations. By setting the determinant equal to zero, one gets a nonlinear algebraic equation for the effective propagation  $K$ . Because the medium is statistical isotropic, we have the same homogeneous set of equation for arbitrary polarization and incident angle of the incident wave. The homogeneous set of equations is

$$Y_\nu^{(s_j)(M)} = -2\pi \sum_{s_l=1}^L n_{s_l} \sum_{n,p} (2n+1) S_p(k, K | R_{s_j, s_l}) \left\{ a(1, n | -1, \nu | p) A(n, \nu, p) T_n^{(s_l)(M)} Y_n^{(M)(s_l)} + a(1, n | -1, \nu | p, p-1) B(n, \nu, p) T_n^{(s_l)(N)} Y_n^{(N)(s_l)} \right\} \quad (16)$$

$$Y_\nu^{(s_j)(N)} = -2\pi \sum_{s_l=1}^L n_{s_l} \sum_{n,p} (2n+1) S_p(k, K | R_{s_j, s_l}) \times \left\{ a(1, n | -1, \nu | p, p-1) B(n, \nu, p) T_n^{(s_l)(M)} Y_n^{(s_l)(M)} + a(1, n | -1, \nu | p) A(n, \nu, p) T_n^{(s_l)(N)} Y_n^{(s_l)(N)} \right\} \quad (17)$$

where  $a(1, n | -1, \nu | p)$  and  $a(1, n | -1, \nu | p, p-1)$  are in terms of Wigner 3-j symbols and can be found on pp. 449-450 of [6]. In (16), (17)

$$A(n, \nu, p) = \frac{\nu(\nu+1) + n(n+1) - p(p+1)}{n(n+1)} \quad (18)$$

$$B(n, \nu, p) = \frac{\sqrt{(n+\nu+p+1)(\nu+p-n)(n+p-\nu)(n+\nu-p+1)}}{n(n+1)} \quad (19)$$

$$S_p(k, K | R_{s_j, s_l}) = -\frac{R_{s_j, s_l}^2}{K^2 - k^2} \left[ kh_p'(kR_{s_j, s_l}) j_p(KR_{s_j, s_l}) - Kh_p(kR_{s_j, s_l}) j_p'(KR_{s_j, s_l}) \right] + \int_{R_{s_j, s_l}}^{\infty} dr r^2 \left[ g_{s_j, s_l}(r) - 1 \right] h_p(kr) j_p(Kr) \quad (20)$$

$$R_{s_j, s_l} = a_{s_j} + a_{s_l} \quad (21)$$

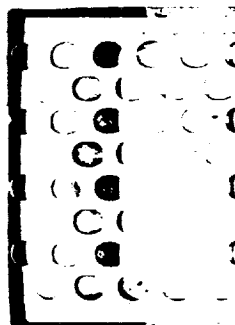
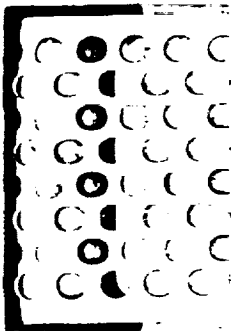
and

$$T_n^{(s_l)(M)} = -\frac{[\rho_{s_l} j_n(\rho_{s_l})]' j_n(\zeta_{s_l}) - [\zeta_{s_l} j_n(\zeta_{s_l})]' j_n(\rho_{s_l})}{[\rho_{s_l} h_n(\rho_{s_l})]' j_n(\zeta_{s_l}) - [\zeta_{s_l} j_n(\zeta_{s_l})]' h_n(\rho_{s_l})} \quad (22)$$

$$T_n^{(s_l)(N)} = -\frac{[\rho_{s_l} j_n(\rho_{s_l})]' \zeta_{s_l}^2 j_n(\zeta_{s_l}) - [\zeta_{s_l} j_n(\zeta_{s_l})]' \rho_{s_l}^2 j_n(\rho_{s_l})}{[\rho_{s_l} h_n(\rho_{s_l})]' \zeta_{s_l}^2 j_n(\zeta_{s_l}) - [\zeta_{s_l} j_n(\zeta_{s_l})]' \rho_{s_l}^2 h_n(\rho_{s_l})} \quad (23)$$

with  $\rho_{s_l} = ka_{s_l}$ ,  $\zeta_{s_l} = k_{s_l} a_{s_l}$ , and  $k_{s_l} = \omega \sqrt{\mu \epsilon_{s_l}}$ , are the Mie scattering  $T$  matrix coefficients for  $\bar{M}$  and  $\bar{N}$  vector spherical waves.

For each species  $s_l$ , we terminate at a multipole  $N_{s_l}$  depending on the radius  $a_{s_l}$  of that species. Thus (12) and (13) form  $N_e$  homogeneous equations for



the  $N_e$  unknowns  $Y_n^{(s_l)(M)}$  and  $Y_n^{(s_l)(N)}$ ,  $n = 1, 2, \dots, N_{s_l}$  and  $s_l = 1, 2, \dots, L$ . Thus  $N_e = \sum_{l=1}^L 2N_{s_l}$ .

The generalized Lorentz-Lorentz law determines the effective propagation  $K$ . Setting the determinant of (16)–(17) equal to zero gives the nonlinear equation for the effective propagation constant  $K$ . After  $K$  is calculated, then the complex transmitted angle  $\theta_t$  and  $K_z$  can be determined from (12)–(15).

The  $N_e$  coefficients  $Y_n^{(s_l)(M)}$  and  $Y_n^{(s_l)(N)}$  are then reduced to only one arbitrary constant that is to be determined by the incident wave. That one equation to determine the arbitrary constant is provided by the generalized Ewald-Oseen extinction theorem which gives a single inhomogeneous equation.

### B. Generalized Ewald-Oseen Extinction Theorem

The generalized Ewald-Oseen extinction theorem is obtained by balancing the incident wave term of the second term of (5) and the term of (11) that is a result of the integral in (5). The result matrix equation can be reduced to one single equation for the set of coefficients  $Y_n^{(s_l)(M)}$  and  $Y_n^{(s_l)(N)}$ . The equation depends on whether the incident wave is vertically polarized or horizontally polarized.

#### 1. Vertical polarized incidence

In this case  $E_{vi} \neq 0$  and  $E_{hi} = 0$ . The coherent transmitted wave is also vertically polarized. The generalized Ewald-Oseen extinction theorem gives rise to the following inhomogeneous equation

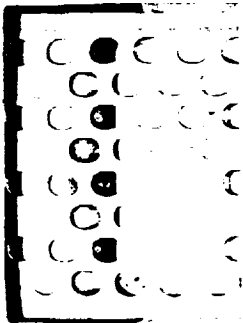
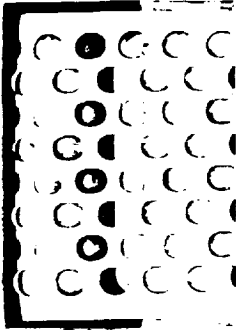
$$\begin{aligned} & \sum_{s_l=1}^L \sum_n n_{s_l} i \frac{(2n+1)}{n(n+1)} \left[ -T_n^{(s_l)(M)} Y_n^{(s_l)(M)(V)} \frac{P_n^1(\cos(\theta_i - \theta_t))}{|\sin(\theta_i - \theta_t)|} \right. \\ & \left. + Y_n^{(s_l)(N)(V)} T_n^{(s_l)(N)} \left\{ \cos(\theta_i - \theta_t) \frac{P_n^1(\cos(\theta_i - \theta_t))}{|\sin(\theta_i - \theta_t)|} + n(n+1) P_n(\cos(\theta_i - \theta_t)) \right\} \right] \\ & = -\frac{(K_z - k_{iz}) k_{iz} k}{2\pi} E_{vi} \end{aligned} \quad (24)$$

where the additional superscript (V) denotes the vertically polarized case. Note that the set of coefficients  $Y_n^{(s_l)(M)(V)}$  and  $Y_n^{(s_l)(N)(V)}$ ,  $n = 1, \dots, N_{s_l}$ ,  $s_l = 1, \dots, L$  have been determined to within one arbitrary constant by the generalized Lorentz-Lorentz law of (16) and (17). Thus (24) provide the last equation that determines all those coefficients uniquely.

#### 2. Horizontal polarized incidence

For this case  $E_{vi} = 0$  and  $E_{hi} \neq 0$ . The coherent transmitted wave is horizontally polarized. The inhomogeneous equation for the generalized Ewald-Oseen extinction theorem is

$$\sum_{s_l=1}^L \sum_n n_{s_l} i \frac{(2n+1)}{n(n+1)} \left[ T_n^{(s_l)(M)} Y_n^{(s_l)(M)(H)} \right]$$



$$\begin{aligned}
& \times \left\{ \cos(\theta_i - \theta_t) \frac{P_n^1(\cos(\theta_i - \theta_t))}{|\sin(\theta_i - \theta_t)|} + n(n+1)P_n(\cos(\theta_i - \theta_t)) \right\} \\
& + T_n^{(s_i)(N)} Y_n^{(s_i)(N)}(H) \left( -\frac{P_n^1(\cos(\theta_i - \theta_t))}{|\sin(\theta_i - \theta_t)|} \right) \\
& = -\frac{(K_z - k_{iz})k_{iz}k}{2\pi} E_{hi} \quad (25)
\end{aligned}$$

where the additional superscript ( $H$ ) denotes horizontal polarization. Thus the homogeneous system of equations of (16), (17) combined with the inhomogeneous equation (25) determines the coefficients  $Y_n^{(s_i)(M)}(H)$  and  $Y_n^{(s_i)(N)}(H)$  uniquely for the use of horizontally polarized incidence.

The case of an incident wave of arbitrary polarization can be calculated by linearly combining the cases of vertical and horizontal polarized incidence.

### C. Bistatic Scattering Coefficients for Incoherent Field

The incoherent field can be studied with the distorted Born approximation or the first order smoothing approximation [4,6]. From the incoherent field, the bistatic-scattering coefficients for the incoherent field can be calculated. The bistatic scattering coefficients are defined by [6]

$$\gamma_{\beta\alpha}(\theta_s, \phi_s; \theta_i, \phi_i) = \frac{4\pi r^2 |\bar{\mathcal{E}}_\beta^s|^2}{|E_\alpha^i|^2 A_0 \cos \theta_i} \quad (26)$$

where  $\bar{\mathcal{E}}_\beta^s$  is the incoherent scattered field of polarization  $\beta$ ,  $E_\alpha^i$  is the incident field of polarization  $\alpha$ ,  $A_0$  is the area of target and  $r$  is the distance of observation point from target. In the following, we shall give the result for bistatic scattering in the plane of incidence  $\phi_s = \phi_i + \pi$  and  $0 \leq \theta_s \leq \pi/2$ . Because of statistical isotropy of random distribution of spherical scatterers, bistatic scattering in the plane of incidence do not have depolarization for vertically polarized incidence or horizontally polarized incidence. Under the distorted Born approximation,  $\gamma_{vv}$  and  $\gamma_{hh}$  are given as follows; for  $0 \leq \theta_s \leq \pi/2$

$$\begin{aligned}
\gamma_{vv}(\theta_s, \phi_s = \pi + \phi_i; \theta_i, \phi_i) &= \frac{4\pi}{k^2} \sum_{s_j} \frac{n_{s_j}}{2K_z'' \cos \theta_i} \left| W_{s_j}^{(V)}(\theta_s, \theta_i) \right|^2 \\
&+ \frac{4\pi}{k^2 \cos \theta_i} \sum_{s_j s_l} n_{s_j} n_{s_l} U_{s_j s_l}(\theta_s, \phi_s = \pi + \phi_i; \theta_i, \phi_i) \\
&\times W_{s_j}^{(V)}(\theta_s, \theta_i) W_{s_l}^{(V)*}(\theta_s, \theta_i) F_d \quad (27)
\end{aligned}$$

$$\begin{aligned}
\gamma_{hh}(\theta_s, \phi_s = \pi + \phi_i; \theta_i, \phi_i) &= \frac{4\pi}{k^2} \sum_{s_j} \frac{n_{s_j}}{2K_z'' \cos \theta_i} \left| W_{s_j}^{(H)}(\theta_s, \theta_i) \right|^2 \\
&+ \frac{4\pi}{k^2 \cos \theta_i} \sum_{s_j s_l} n_{s_j} n_{s_l} U_{s_j s_l}(\theta_s, \phi_s = \pi + \phi_i; \theta_i, \phi_i) \\
&\times W_{s_j}^{(H)}(\theta_s, \theta_i) W_{s_l}^{(H)*}(\theta_s, \theta_i) F_d \quad (28)
\end{aligned}$$

$$\begin{aligned}
W_{s_j}^{(V)}(\theta_s, \theta_i) = & \sum_n (-1)^n \frac{(2n+1)}{n(n+1)} \left\{ T_n^{(s_j)(M)} Y_n^{(s_j)(M)(V)} \frac{P_n^1(\cos(\theta_s - \theta_i))}{|\sin(\theta_s - \theta_i)|} \right. \\
& + T_n^{(s_j)(N)} Y_n^{(s_j)(N)(V)} \left( \cos(\theta_s - \theta_i) \frac{P_n^1(\cos(\theta_s - \theta_i))}{|\sin(\theta_s - \theta_i)|} \right. \\
& \left. \left. + n(n+1) P_n(\cos(\theta_s - \theta_i)) \right) \right\} \quad (29)
\end{aligned}$$

$$\begin{aligned}
W_{s_j}^{(H)}(\theta_s, \theta_i) = & \sum_n (-1)^n \frac{(2n+1)}{n(n+1)} \left\{ T_n^{(s_j)(N)} Y_n^{(s_j)(N)(H)} \frac{P_n^1(\cos(\theta_s - \theta_i))}{|\sin(\theta_s - \theta_i)|} \right. \\
& + T_n^{(s_j)(M)} Y_n^{(s_j)(M)(H)} \left( \cos(\theta_s - \theta_i) \frac{P_n^1(\cos(\theta_s - \theta_i))}{|\sin(\theta_s - \theta_i)|} \right. \\
& \left. \left. + n(n+1) P_n(\cos(\theta_s - \theta_i)) \right) \right\} \quad (30)
\end{aligned}$$

and

$$\begin{aligned}
U_{s_j s_l}(\theta_s, \phi_s = \pi + \phi_i; \theta_i, \phi_i) &= \frac{1}{2 \operatorname{Im}(K_z)} \int_{-\infty}^{\infty} d\bar{r} \left[ g_{s_j s_l}(\bar{r}) - 1 \right] e^{i(\operatorname{Re} \bar{K}_d - \bar{K}_s) \cdot \bar{r}} \\
&= \frac{(2\pi)^3}{2 \operatorname{Im}(K_z)} H_{s_j s_l}(\bar{p} = -\operatorname{Re} \bar{K}_d + \bar{k}_s) \quad (31)
\end{aligned}$$

where superscript double prime denotes imaginary part. In (31),  $\bar{K}_d$  is given by (8), (12)–(15) and

$$\bar{k}_s = k(\sin \theta_s \cos \phi_s \hat{x} + \sin \theta_s \sin \phi_s \hat{y} + \cos \theta_s \hat{z}) \quad (32)$$

is the wave vector of the scattered wave in region 0. In (31)  $H_{s_j s_l}$ ,  $s_j, s_l = 1, 2, \dots, L$  is the Fourier transform of the cross pair distribution function  $g_{s_j s_l}$  minus 1. It is also called structure factor.

$$H_{s_j s_l}(\bar{p}) = \frac{1}{(2\pi)^3} \int_{-\infty}^{\infty} d\bar{r} [g_{s_j s_l}(\bar{r}) - 1] e^{-i\bar{p} \cdot \bar{r}} \quad (33)$$

Thus the bistatic scattering coefficient is proportional to the Fourier transform of the cross pair distribution function, a concept that has been used extensively in the investigation of molecular structures of liquids and amorphous solids by X-rays [22].

For multiple sizes of spherical particles, the cross pair distribution function  $g_{s_j s_l}$  are isotropic, so that  $g_{s_j s_l}(\bar{r})$  depends on  $|\bar{r}|$  only. Hence, the cross structure factor  $H_{s_j s_l}(\bar{p})$  also depends on  $|\bar{p}|$  only. It is useful to note that under the Percus-Yevick approximation, closed form expressions are available [18,19,22] for  $H_{s_j s_l}(\bar{p})$ ,  $s_j, s_l = 1, 2, \dots, L$ .

In (27) and (28)

$$F_d = (1 - e^{-2K_z'' d}) \quad (34)$$

where  $K_z'' = \operatorname{Im}(K_z)$ .

We have inserted in (34) the thickness  $d$  of the layer containing random discrete scatterers. The results of (34) only include volume scattering and ignores any possible reflections from the bottom boundary.

### III. NUMERICAL RESULTS AND DISCUSSION

In this section, we shall illustrate the numerical results of the effective propagation constants and backscattering coefficients using parameters of snow. The results are illustrated with the Rayleigh size distribution which is a special case of the modified gamma size distribution. The size distribution is represented by  $n(a)$ , which is the number of particles per unit volume with radii between  $a$  and  $a+da$ . It is given by

$$n(a) = \frac{\pi f a}{16 \langle a \rangle^5} \exp\left(-\frac{\pi a^2}{4 \langle a \rangle^2}\right) \quad (35)$$

where  $\langle a \rangle$  is the mean radius. The fractional volume and the mean radius are defined by

$$f = \int_0^\infty da \frac{4\pi}{3} a^3 n(a) \quad (36)$$

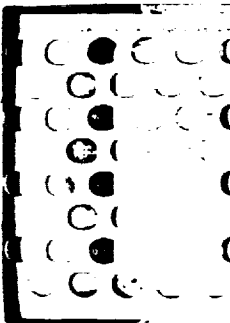
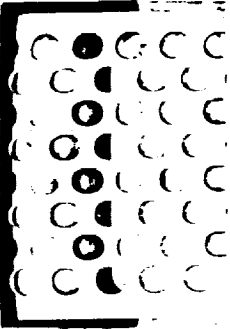
$$\langle a \rangle = \frac{\int_0^\infty da a n(a)}{\int_0^\infty da n(a)} \quad (37)$$

$$a_m = \sqrt{\frac{2}{\pi}} \langle a \rangle \quad (38)$$

Thus, given the fractional volume  $f$ , the Rayleigh size distribution contains only one parameter, viz., the mean radius. In (38)  $a_m$  is the mode radius where the size distribution is at a maximum [20], and as indicated in (38), is approximately equal to  $0.798 \langle a \rangle$ . In our numerical calculations of Figs. 2 to 11, we discretize the Rayleigh size distribution into 20 different equally spaced sizes (i.e.  $L = 20$  species). The pair distribution functions for a medium with 20 sizes are then calculated by the Percus-Yevick approximation [20]. The maximum size for these 20 sizes is chosen such that at least 99.7% of the scattering contributions and the fractional volume of particles are included. That usually occurs around 2.5 to 3 times the mean radius. Comparison will be made between the scattering of a medium with Rayleigh size distribution of a specified value of  $\langle a \rangle$  and the case of monodisperse particles with radii equal to that same value. The results of QCA will also be compared with that of independent scattering. For the case of independent scattering, the extinction rate is

$$(\kappa_e)_{\text{independent}} = -\frac{2\pi}{k^2} \sum_{s_j=1}^L n_{s_j} \sum_n (2n+1) \text{Re} \left[ T_n^{(M)s_j} + T_n^{(N)s_j} \right] \quad (39)$$

In Figs. 2 and 3, we plot respectively the effective loss tangent  $2K_i/K_r$  and the normalized phase velocity  $k/K_r$  as a function of fractional volume at frequency = 37 GHz for two Rayleigh size distributions with  $\langle a \rangle = 0.05$  cm and  $\langle a \rangle = 0.09$  cm. We note that the effective loss tangents first increase with fractional volume, rise to maxima and then decrease with further increase in fractional volume. These are consistent with controlled optical experiments [3] and controlled microwave experiments [26]. The peak of the larger size of  $\langle a \rangle = 0.09$  cm occurs at  $f = 0.19$  and the peak for  $\langle a \rangle = 0.05$  cm occurs at  $f = 0.16$ . This indicates that scattering





by larger particles are "more independent." "More independent" means that for scattering by large particles, the "hole correction" for distribution functions very often are sufficient to characterize the scattering [6]. Figure 3 shows that the phase velocity decreases with fractional volume with smaller velocity for larger particles indicating that scattering decreases phase velocity. In Fig. 4, the backscattering coefficients are plotted as a function of fractional volume for a layer thickness of  $d = 3$  cm. The backscattering coefficients are  $\sigma_{\beta\beta} = \cos\theta_i \gamma_{\beta\beta}$  with  $\beta = v, h$ . A small thickness is chosen because the model of incoherent scattering is limited to distorted Born approximation which is valid only for small optical thickness. The associated extinction rates of Fig. 2 show that multiple scattering of incoherent waves become important for thickness larger than 3 cm as the optical thickness becomes large. The results of Fig. 4 indicate that backscattering coefficient can be as large as  $-4$  dB for a small layer thickness of  $d = 3$  cm.

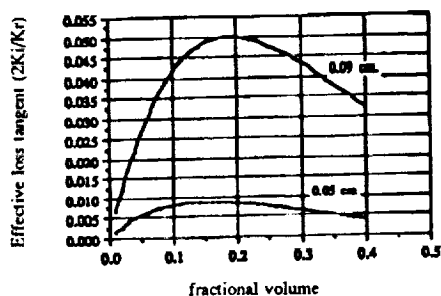
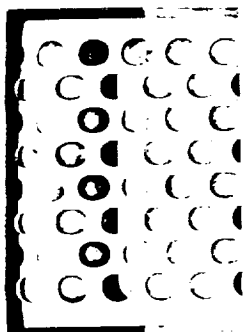


Figure 2. Effective loss tangent  $2K_i/K_r$  of QCA as a function of fractional volume. Frequency is at 37 GHz. The permittivity of the particles is  $\epsilon_s = (3.2 + i0.001)\epsilon_0$ . Two cases of Rayleigh size distributions are considered with  $\langle a \rangle = 0.05$  cm and  $\langle a \rangle = 0.09$  cm.

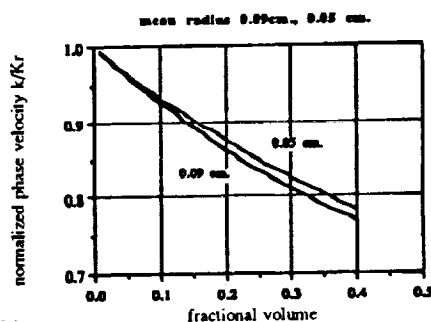
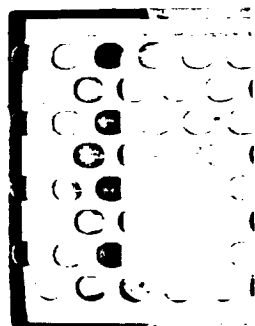


Figure 3. Normalized phase velocity  $k/K_r$  of QCA as a function of fractional volume. Frequency is at 37 GHz. The permittivity of the particles is  $\epsilon_s = (3.2 + i0.001)\epsilon_0$ . Two cases of Rayleigh size distributions are considered with  $\langle a \rangle = 0.05$  cm and  $\langle a \rangle = 0.09$  cm.



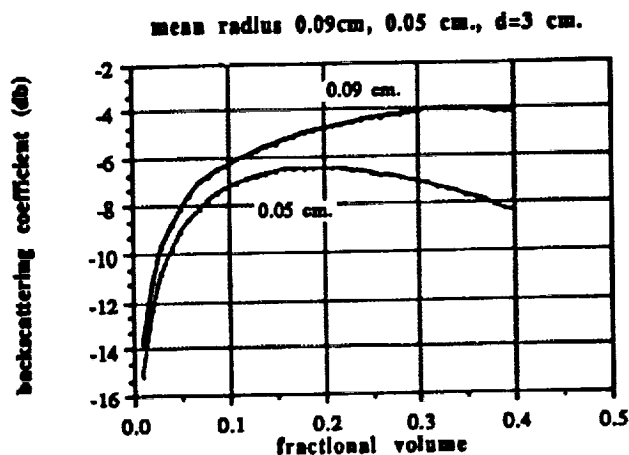
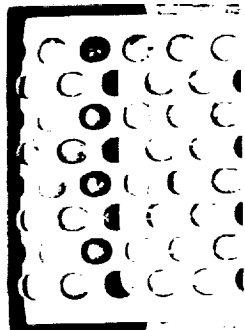
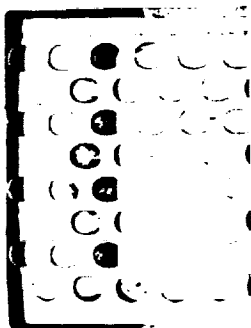


Figure 4. Backscattering coefficient  $\sigma_{hh}$  in dB of QCA as a function of fractional volume. Frequency is at 37 GHz. The permittivity of the particles is  $\epsilon_s = (3.2 + i0.001)\epsilon_0$ . Two cases of Rayleigh size distributions are considered with  $\langle a \rangle = 0.05$  cm and  $\langle a \rangle = 0.09$  cm. The layer thickness is  $d = 3$  cm and incident angle is  $30^\circ$ .

In Figs. 5, 6, and 7, we show the coherent wave attenuation rates for a smaller mean grain radius of 0.035 cm. The corresponding mode radius is 0.0279 cm. Figure 5 compares the extinction rate  $2K_i$  between independent scattering and QCA. We note that attenuation rate of independent scattering is larger than QCA. The results show that the extinction rate first increases rapidly with frequency as in Rayleigh scattering. Then it departs from Rayleigh scattering around 20 GHz and starts to gradually level off. This indicates the importance of including Mie scattering effects beyond 20 GHz for  $\langle a \rangle = 0.035$  cm. Figure 6 compares the results of QCA between the extinction rates of monodisperse particles with radii = 0.035 cm and the case of Rayleigh size distribution with  $\langle a \rangle = 0.035$  cm. We note that the case of Rayleigh size distribution has a considerably larger scattering rate than monodisperse case. This indicates the importance of including size distribution in modelling scattering from realistic geophysical terrain when grain sizes are small. It also means that in laboratory controlled experiments when particle sizes are made to be close to monodisperse, the measured scattering can be substantially less. The numerical results indicate that the extinction rate is at  $1.056 \text{ cm}^{-1}$  based on Rayleigh size distribution at frequency = 95 GHz meaning that there is strong multiple scattering of incoherent waves at such high frequency even for moderate snow layer thicknesses. Figure 7 shows the results of HH backscattering coefficient for a layer thickness of  $d = 10$  cm. It shows that distorted Born backscattering can be as large as 0 dB at 60 GHz with  $\langle a \rangle = 0.035$  cm. The curves show saturation effects due to the limitations of distorted Born approximation. We expect that if multiple scattering of incoherent waves are included, the backscattering should continue to increase above 0 dB.



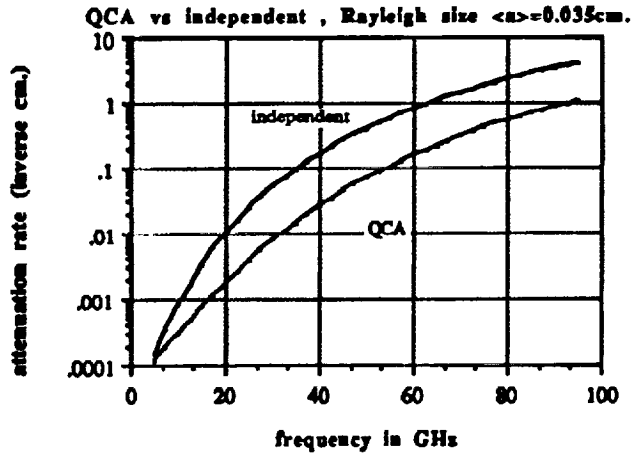
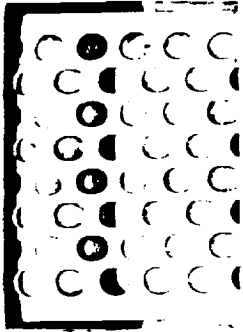


Figure 5. Coherent wave attenuation rate  $2K_i$  in  $\text{cm}^{-1}$  as a function of frequency. The permittivity of the particles is  $\epsilon_s = (3.2 + i0.001)\epsilon_0$ . Rayleigh size distribution is considered with  $\langle a \rangle = 0.035 \text{ cm}$  and fractional volume  $f = 0.3$ . The cases of independent scattering and QCA are compared.

QCA (single size  $a=0.035 \text{ cm}$ . vs Rayleigh size  $\langle a \rangle = 0.035 \text{ cm}$ .)

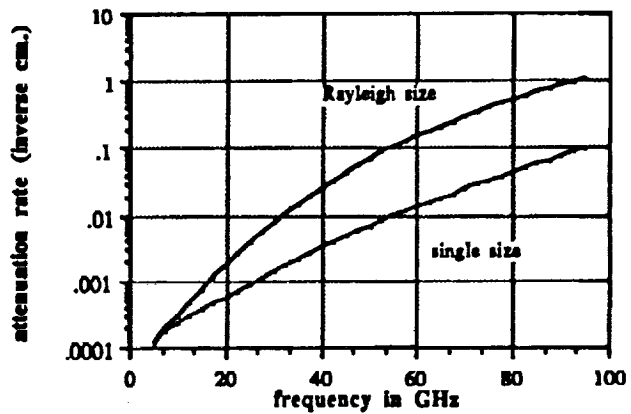
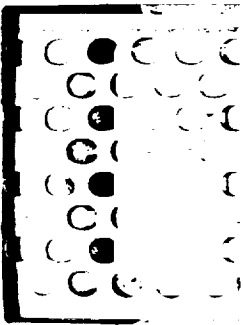


Figure 6. Coherent wave attenuation rate  $2K_i$  in  $\text{cm}^{-1}$  under QCA as a function of frequency. The permittivity of the particles is  $\epsilon_s = (3.2 + i0.001)\epsilon_0$ . The fractional volume is  $f = 0.3$ . The cases of identical sizes of  $a = 0.035 \text{ cm}$  and Rayleigh size distribution with  $\langle a \rangle = 0.035 \text{ cm}$  are compared.



QCA ( $d=10$  cm., single size  $a=0.035$  cm. vs Raleigh size  $\langle a \rangle=0.035$  cm.)

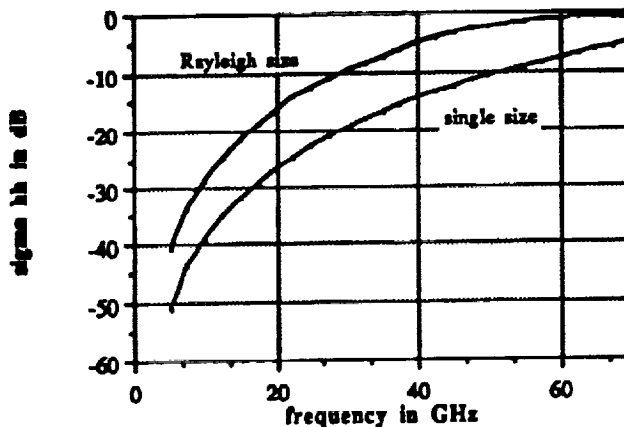
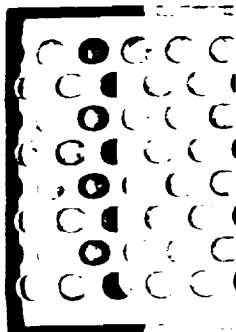


Figure 7. Backscattering coefficient  $\sigma_{hh}$  in dB of QCA as a function of frequency. The permittivity of the particles is  $\epsilon_s = (3.2 + i0.001)\epsilon_0$ . The layer thickness is  $d = 10$  cm and incident angle is  $30^\circ$ . The cases of identical sizes of  $a = 0.035$  cm and Rayleigh size distribution with  $\langle a \rangle = 0.035$  cm are compared.

In Figs. 8, 9 and 10, the results for the cases of a larger mean grain radius of 0.075 cm are shown. The corresponding mode radius is 0.0598 cm. Figure 8 shows that the extinction rate of independent scattering is still larger than that of QCA. However the two curves are much closer than that of Figure 5 showing that scattering by larger particles are "more independent." At frequency = 95 GHz, QCA and independent scattering are almost the same. Figure 9 shows that the Rayleigh size distribution case is considerably larger than the monodisperse case. Strong multiple scattering is to be expected as the extinction rates of QCA for Rayleigh size case are large. Figure 10 show the HH backscattering coefficients of a snow layer of thickness  $d = 1$  cm. The small layer thickness is chosen to satisfy the validity condition of small optical thickness for distorted Born approximation. The saturation effect in Fig. 10 is a demonstration of the limitation of the distorted Born approximation. Nevertheless, the backscattering coefficients are quite large in view of the small layer thickness of  $d = 1$  cm. In Fig. 11, the VV and HH backscattering coefficients are plotted as a function of incident angles at frequency = 37 GHz and  $d = 10$  cm. There is a gradual decrease with incident angle. There is little difference between VV and HH with the HH return slightly larger than VV.



QCA vs independent, Rayleigh size  $\langle a \rangle = 0.075$  cm.

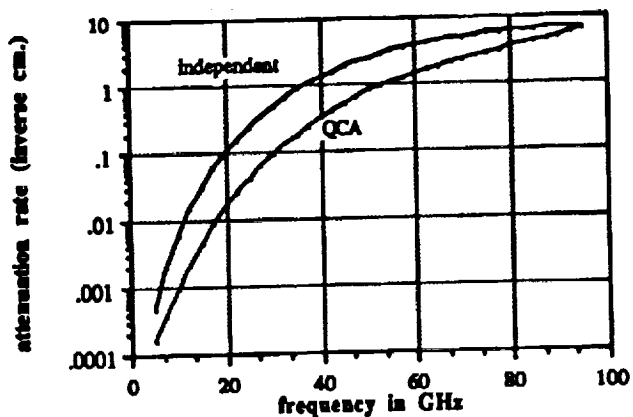


Figure 8. Coherent wave attenuation rate  $2K_i$  in  $\text{cm}^{-1}$  as a function of frequency. The permittivity of the particles is  $\epsilon_s = (3.2 + i0.001)\epsilon_0$ . Rayleigh size distribution is considered with  $\langle a \rangle = 0.075$  cm and fractional volume  $f = 0.3$ . The cases of independent scattering and QCA are compared.

qca (single size  $a=0.075$  cm., and Rayleigh size  $\langle a \rangle = 0.075$  cm.)

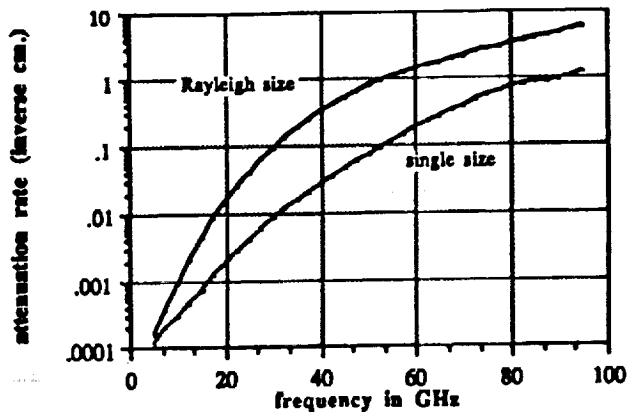
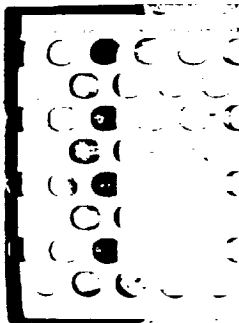
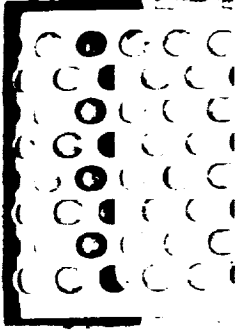


Figure 9. Coherent wave attenuation rate  $2K_i$  in  $\text{cm}^{-1}$  of QCA as a function of frequency. The permittivity of the particles is  $\epsilon_s = (3.2 + i0.001)\epsilon_0$ . The fractional volume is  $f = 0.3$ . The cases of identical sizes of  $a = 0.075$  cm and Rayleigh size distribution with  $\langle a \rangle = 0.075$  cm are compared.





QCA ( $d = 1$  cm.; single size  $a=0.075$  cm.; Rayleigh size  $\langle a \rangle=0.075$  cm.)

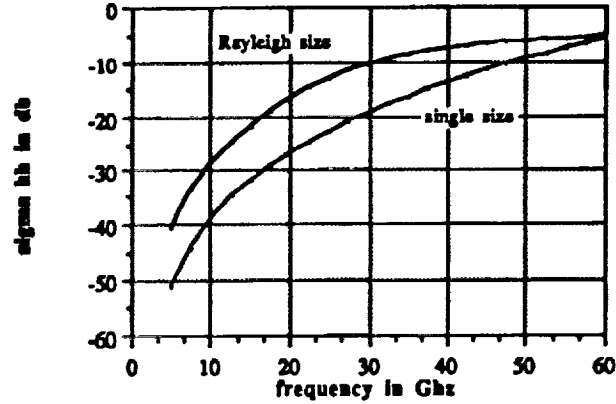


Figure 10. Backscattering coefficient  $\sigma_{hh}$  in dB of QCA as a function of frequency. The permittivity of the particles is  $\epsilon_s = (3.2 + i0.001)\epsilon_0$ . The layer thickness is  $d = 1$  cm and incident angle is  $30^\circ$ . The cases of identical sizes of  $a = 0.075$  cm and Rayleigh size distribution with  $\langle a \rangle = 0.075$  cm are compared.

VV and HH returns,  $d=10$  cm., Rayleigh size  $\langle a \rangle=0.075$  cm.

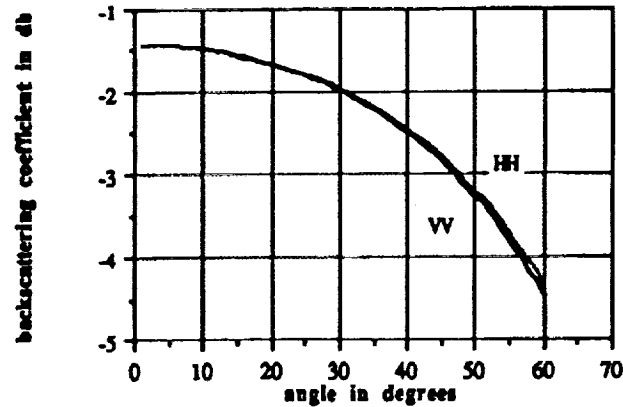
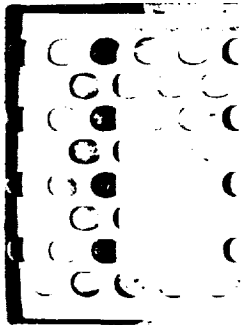


Figure 11. Backscattering coefficient  $\sigma_{vv}$  and  $\sigma_{hh}$  in dB of QCA as a function of incident angle. The permittivity of the particles is  $\epsilon_s = (3.2 + i0.001)\epsilon_0$ . The layer thickness is  $d = 10$  cm. Frequency is at 37 GHz. The cases of Rayleigh size distribution with  $\langle a \rangle = 0.075$  cm is considered.



IV. COMPARISON WITH EXTINCTION MEASUREMENTS OF DRY SNOW BETWEEN 18 GHZ AND 90 GHZ

In this section, we apply the dense media QCA-PY-Mie theory to compare with extinction measurements of dry snow. Dry snow is a mixture of ice grains and air. Hallikainen et al. [24] measured the extinction behavior of different types of dry snow at four frequencies: 18 GHz, 35 GHz, 60 GHz and 90 GHz. Thus, it is important to match the data for a sample over the entire frequency range with one set of physical parameters. In this section, we shall match the data of one sample (sample number 9 [24]) of large grains. Other samples are being studied and comparisons will be reported in the future.

Recently, grain size distributions of dry snow have been measured extensively [27]. Dry snow can be divided into new snow and old snow. New snow has smaller mean size and smaller standard deviation while old snow has larger grain size and larger standard deviation. The standard deviation of grain size radius can be several times larger than the mode radius showing that snow has a broad grain size distribution. The maximum grain diameter is between 3 mm to 4 mm. It is also observed that the number ratio of large grains to grains with mean size is about 1 to 300 [27].

In the following, we shall compare with the snow data for sample 9 [24] with ground truth of mean grain diameter = 1 mm and snow density = 0.385 gm/cc. This corresponds to a fractional volume of 0.423. The reported measurements of extinction are 10.2 dB/m, 58.8 dB/m, 247.2 dB/m and 304.0 dB/m respectively at frequencies of 18 GHz, 35 GHz, 60 GHz and 90 GHz. Comparisons are made with QCA-PY-Mie theory based on two size distributions: the modified gamma size distribution and the histogram (Fig. 12) based on information as discussed above [27]

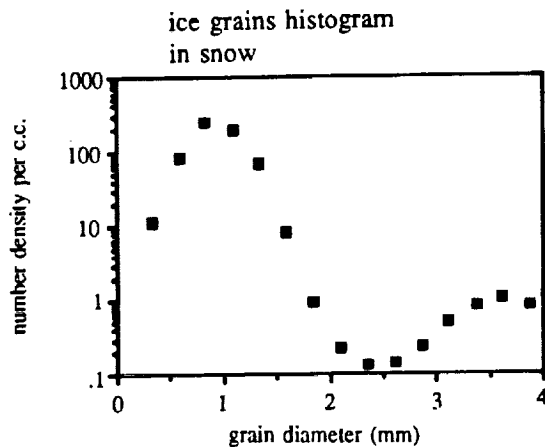
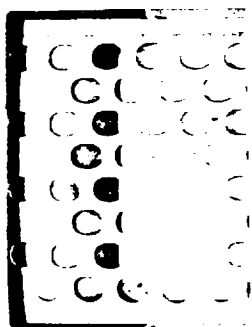
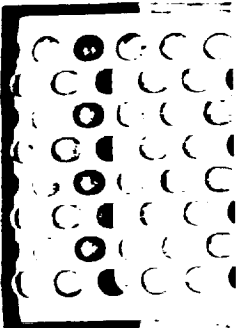


Figure 12. The ice grain size histogram in snow in number per c.c. as a function of grain diameter. The histogram is used for QCA-PY-Mie theory in Fig. 14. There are 15 sizes, with mean grain radius of 0.0479 cm and fractional volume of 0.4134.



The modified gamma size distribution is

$$n(a) = K_1 a^P \exp(-K_2 a^Q) \quad (39)$$

with

$$K_2 = \left( \frac{\Gamma\left(\frac{P+2}{Q}\right)}{\langle a \rangle \Gamma\left(\frac{P+1}{Q}\right)} \right)^Q \quad (40)$$

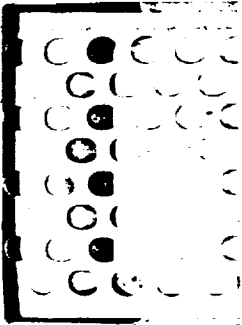
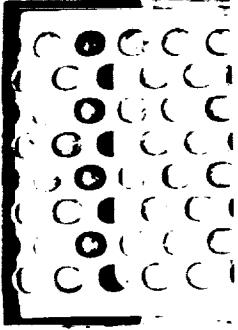
$$K_1 = \frac{3fQ}{4\pi\Gamma\left(\frac{P+4}{Q}\right)} (K_2)^{\frac{P+4}{Q}} \quad (41)$$

Thus, the size distributions have four parameters  $P$ ,  $Q$ ,  $K_1$ , and  $K_2$ . However,  $K_2$  and  $K_1$  can be expressed in terms of mean radius  $\langle a \rangle$  and fractional volume  $f$  as indicated in (40)–(41). Thus the alternative four parameters are  $\langle a \rangle$ ,  $f$ ,  $P$  and  $Q$ .

The second size distribution that we used is in Fig. 12 which shows the histogram number density (number per c.c.) for 15 sizes with mean grain radius of 0.0479 cm and fractional volume of 0.4134. Note that there are large grains between 3 mm to 4 mm with the number ratio to grains of mean size of about 1 to 300 [27].

In Fig. 13, we make a comparison with the data based on the modified gamma size distribution with  $P = 1$ ,  $Q = 1.4$ ,  $\langle a \rangle = 0.05$  cm. and  $f = 0.423$ . The permittivity of ice grains chosen are  $\epsilon_s = 3.2\epsilon_0 + i\epsilon_s''$  with  $\epsilon_s''/\epsilon_0 = 0.007, 0.009, 0.011$  and  $0.014$  respectively at 18 GHz, 35 GHz, 60 GHz and 90 GHz which corresponds to a salinity of 0.12 parts per thousand [28]. The results of independent scattering are also shown for comparison. The results in figure 13 show that the independent scattering results are larger than the data while the QCA-PY-Mie theory shows a reasonable match based on the modified gamma size distribution.

In Fig. 14, we make a comparison with data based on the histogram size distribution of Fig. 12 and using the same permittivity of ice grains as in Fig. 13. The agreement is good. It seems that with size distribution, the QCA-PY-Mie theory can explain the frequency dependence of the extinction of dry snow between 18 GHz and 90 GHz. The results of independent scattering are also shown for comparison. Future comparisons will be made when the size distributions of ice grains in snow become available [27]. Note that we have used the Percus-Yevick pair functions for non-interacting particles without mutual force. It seems that ice grains may have sticking force that may affect the pair distribution functions. Besides QCA, the quasicrystalline approximation with coherent potential [6,8] should be used. Monte-Carlo simulations of extinction rate can also be made based on the solution of Maxwell's equations [29].





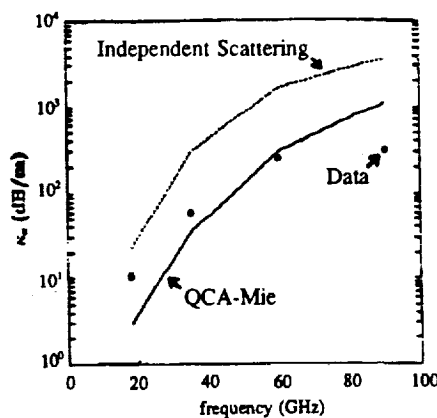
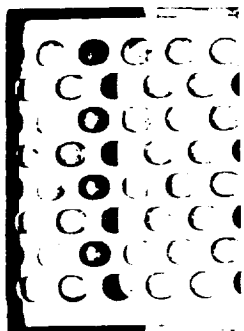


Figure 13. Comparison between QCA-PY-Mie theory and independent scattering with snow extinction data at 18 GHz, 35 GHz, 60 GHz, and 90 GHz of Hallikanen et al. [24] with ground truth of mean grain diameter of 1 mm and snow density=0.385 gm/cc. The theory is based on the modified gamma size distribution with  $P = 1$ ,  $Q = 1.4$ ,  $\langle a \rangle = 0.05$  cm, and  $f = 0.423$ . The permittivity of ice grains chosen are  $\epsilon = 3.2\epsilon_0 + i\epsilon_s$  with  $\epsilon_s''/\epsilon_0 = 0.007, 0.009, 0.011$  and  $0.014$  respectively at 18 GHz, 35 GHz, 60 GHz, and 90 GHz which corresponds to a salinity of 0.12 parts per thousand [28].

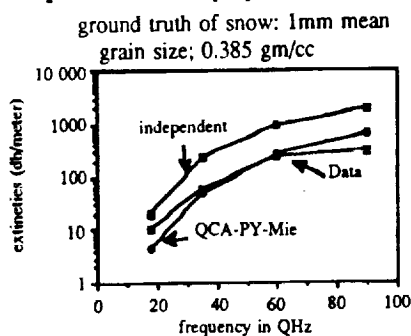
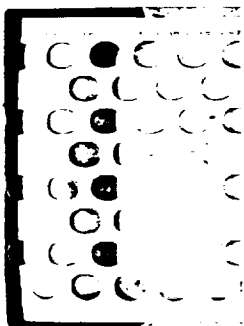


Figure 14. Comparison between QCA-PY-Mie theory and independent scattering with snow extinction data at 18 GHz, 35 GHz, 60 GHz, and 90 GHz of Hallikanen et al. [24] with ground truth of mean grain diameter of 1 mm and snow density=0.385 gm/cc. The theory is based on the histogram of Fig. 12 with  $\langle a \rangle = 0.0479$  cm, and  $f = 0.4134$ . The permittivity of ice grains chosen are  $\epsilon_s = 3.2\epsilon_0 + i\epsilon_s''$  with  $\epsilon_s''/\epsilon_0 = 0.007, 0.009, 0.011$ , and  $0.014$ , respectively, at 18 GHz, 35 GHz, 60 GHz, and 90 GHz which corresponds to a salinity of 0.12 parts per thousand [28].



## V. CONCLUSIONS

In this paper, we have illustrated the importance of dense medium theory of correlated Mie scattering for studying snow cover at microwave and millimeter wave frequencies above 15 GHz. We have also demonstrated the importance of including size distributions as there are large difference between the polydisperse and the monodisperse cases. The importance of polydispersions has long been noted [17], particularly at low frequency when scattering is proportional to particle size to the sixth power. Based on size distributions, the dense medium theory is able to account for the frequency dependence of extinction of dry snow between 18 GHz and 90 GHz. The calculations also show that extinction rates are large for dense medium so that multiple scattering effects become important even for small layer thicknesses. The calculation of the incoherent wave in this paper has been limited to that of distorted Born approximation. The subject of multiple scattering for the incoherent wave including the effects of correlated Mie scattering should be an important future subject for snow cover scattering beyond 15 GHz.

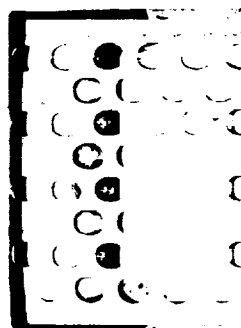
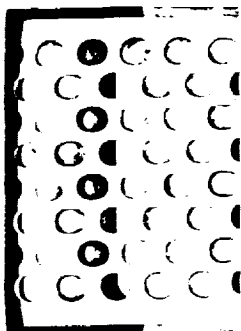
## ACKNOWLEDGMENTS

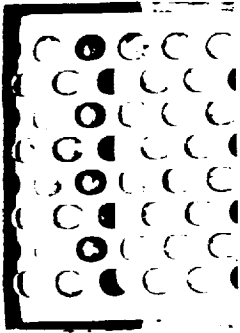
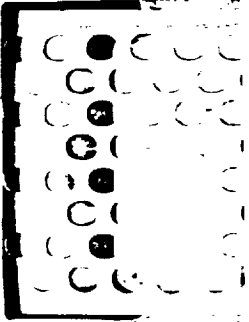
The research in this paper has been supported by the Army Research Office, NASA and the National Science Foundation. The authors would like to thank R. West, D. Winebrenner and J. C. Shi for stimulating discussions.

The Editor thanks A. K. Fung and two anonymous Reviewers for reviewing the paper.

## REFERENCES

1. Twersky, V., "Coherent electromagnetic waves in pair-correlated random distributions of aligned scatterers," *J. Math. Phys.*, Vol. 19, 215-230, 1978.
2. Tsang, L., and J. A. Kong, "Effective propagation constant for coherent electromagnetic waves in media embedded with dielectric scatterer," *J. Appl. Phys.*, Vol. 53, 7162-7173, 1982.
3. Ishimaru, A., and Y. Kuga, "Attenuation constant of a coherent field in a dense distribution of particles," *J. Opt. Soc. Am.*, Vol. 72, 1317-1320, 1982.
4. Tsang, L., and J. A. Kong, "Scattering of electromagnetic waves from a half space of densely distributed dielectric scatterers," *Radio Science*, Vol. 18, 1260-1272, 1983.
5. Varadan, V. K., V. N. Bringi, V. V. Varadan, and A. Ishimaru, "Multiple scattering theory for waves in discrete random media and comparison with experiments," *Radio Science*, Vol. 18, 321-327, 1983.
6. Tsang, L., J. A. Kong, and R. T. Shin, *Theory of Microwave Remote Sensing*, Wiley-Interscience, New York, 1985.
7. Tsang, L., and A. Ishimaru, "Radiative wave equation for vector electromagnetic propagation in dense non-tenuous media," *J. Electro. Waves Applic.*, Vol. 1, 59-72, 1987.
8. Ding, K. H., and L. Tsang, "Effective propagation constants in media with densely distributed dielectric particles of multiple sizes and permittivities," Chapter 3 of *Progress in Electromagnetic Research*, Vol. 1, ed. J. A. Kong, 241-295, 1989.
9. Wen, B., L. Tsang, D. P. Winebrenner, and A. Ishimaru, "Dense medium radiative transfer theory: comparison with experiment and application to microwave remote sensing and polarimetry," *IEEE Trans. Geosci. Remote Sensing*, Vol. 28, 46-59,



- 
- 
10. Kuga, Y., F. T. Ulaby, T. F. Haddock, and R. DeRoo, "Millimeter wave radar scattering from snow: Part I Radiative transfer model," *Radio Science*, Vol. 26, No. 2, 329-341, 1991.
  11. Ulaby, F. T., T. F. Haddock, R. Austin, and Y. Kuga, "Millimeter wave radar scattering from snow: Part II—comparison of theory with experimental observations," *Radio Science*, Vol. 26, No. 2, 343-351, 1991.
  12. Zhu, P. A., A. K. Fung, and K. W. Wong, "Effective propagation constants in dense discrete random media under effective medium approximation," *Radio Science*, Vol. 22, 234-250, 1987.
  13. Tsang, L., "Dense media radiative transfer theory for dense discrete random media with spherical particles of multiple sizes and permittivities," *Progress in Electromagnetic Research*, in press, 1991.
  14. Ishimaru, A., *Wave Propagation and Scattering in Random Media*, Vol. 2, Academic Press, New York, 1978.
  15. Kuga, Y., and A. Ishimaru, "Retroreflectance from a dense distribution of spherical particles," *J. Opt. Soc. Am. A*, Vol. 1, 831-835, 1984.
  16. West, R., L. Tsang, and D. P. Winebrenner, "Dense medium radiative transfer theory for two scattering layers with a Rayleigh distribution of particle sizes," to be published, 1991.
  17. Deirmendjian, D., *Electromagnetic Scattering on Spherical Polydispersions*, Elsevier, New York, 1969.
  18. Baxter, R. J., "Ornstein-Zernike relation for a disordered fluid," *Australian J. of Physics*, Vol. 21, 563-569, 1968.
  19. Baxter, R. J., "Ornstein-Zernike relation and Percus-Yevick approximation for fluid mixtures," *Journal of Chemical Physics*, Vol. 52, 4559-4562, 1970.
  20. Ding, K. H., and L. Tsang, "Effective propagation constants and attenuation rates in media of densely distributed coated dielectric particles with size distributions," *Journal of Electromagnetic Waves and Applications*, Vol. 5, No. 2, 117-142, 1991.
  21. Born, M., and E. Wolf, *Principles of Optics*, 5th ed., Pergamon Press, New York, 1975.
  22. Waseda, Y., *The Structure of Non-Crystalline Materials, Liquids and Amorphous Solids*, McGraw Hill, New York, 1980.
  23. Ding, K. H., C. E. Mandt, L. Tsang, and J. A. Kong, "Monte Carlo simulations of pair distribution functions with multiple sizes in dense discrete random media," submitted to *Journal of Electromagnetic Waves and Applications*, 1991.
  24. Hallikainen, M. T., F. T. Ulaby, and T. van Deventer, "Extinction coefficient of dry snow at microwave and millimeter wave frequencies," *IEEE Trans. on Geoscience and Remote Sensing*, Vol. 25, 737-745, 1987.
  25. Fikioris, J. G., and P. C. Waterman, "Multiple scattering of waves II, hole-corrections in the scalar case," *J. Math. Phys.*, Vol. 5, 1413-1420, 1964.
  26. Mandt, C., "Microwave propagation and scattering in a dense distribution of spherical particles," M.S. thesis, Department of Electrical Engineering, University of Washington, 1987.
  27. Shi, J. C., private communication, U. C. Santa Barbara.
  28. Matzler, C., and U. Wegmuller, "Dielectric properties of fresh-water ice at microwave frequencies," *J. Phys. D.*, Vol. 20, 1623-1630, 1987.
  29. Tsang, L., C. Mandt, and K. H. Ding, "Monte-Carlo simulations of extinction rate of dense media based on solution of Maxwell's equations," to be published, 1991.

Leung Tsang is Professor of Electrical Engineering at the University of Washington, Seattle, Washington. He received all his degrees (B.S., M.S., and Ph.D.) from the Department of Electrical Engineering and Computer Science of the Massachusetts Institute of Technology, Cambridge, Massachusetts. He is the coauthor of the book, *Theory of Microwave*

*Remote Sensing*, (Wiley-Interscience, New York 1985). He is an associate editor of *Radio Science*, an associate editor of *IEEE Trans. on Geoscience and Remote Sensing*, an editor of *Journal of Electromagnetic Waves and Applications* and also on the editorial board of *Waves in Random Media*. He is a fellow of IEEE.

J. A. Kong is Professor of Electrical Engineering and Chairman of Area IV on Energy and Electromagnetic Systems in the Department of Electrical Engineering and Computer Science at the Massachusetts Institute of Technology in Cambridge, Massachusetts. His research interest is in the field of electromagnetic wave theory and applications. He has published 7 books and over 300 refereed journal and conference papers, and is the Editor of the Wiley Series in Remote Sensing, and Chief Editor of the Elsevier book series of Progress In Electromagnetics Research (PIER).

